PAPER

Overview of experimental results and code validation activities at Alcator C-Mod

Nucl. Fusion **53** (2013) 104004 (14pp) doi:10.1088/0029-5515/53/10/104004

Overview of experimental results and code validation activities at Alcator C-Mod

M. Greenwald[1], A. Bader[2], S. Baek[1], H. Barnard[1], W. Beck[1], W. Bergerson[3], I. Bespamyatnov[4], M. Bitter[5], P. Bonoli[1], M. Brookman[4], D. Brower[3], D. Brunner[1], W. Burke[1], J. Candy[6], M. Chilenski[1], M. Chung[1], M. Churchill[1], I. Cziegler[10], E. Davis[1], G. Dekow[1], L. Delgado-Aparicio[5], A. Diallo[5], W. Ding[3], A. Dominguez[5], R. Ellis[5], P. Ennever[1], D. Ernst[1], I. Faust[1], C. Fiore[1], E. Fitzgerald[1], T. Fredian[1], O.E. Garcia[8], C. Gao[1], M. Garrett[1], T. Golfinopoulos[1], R. Granetz[1], R. Groebner[6], S. Harrison[5], R. Harvey[11], Z. Hartwig[1], K. Hill[5], J. Hillairet[14], N. Howard[1], A.E. Hubbard[1], J.W. Hughes[1], I. Hutchinson[1], J. Irby[1], A.N. James[7], A. Kanojia[1], C. Kasten[1], J. Kesner[1], C. Kessel[5], R. Kube[8], B. LaBombard[1], C. Lau[1], J. Lee[1], K. Liao[4], Y. Lin[1], B. Lipschultz[1], Y. Ma[1], E. Marmar[1], P. McGibbon[1], O. Meneghini[6], D. Mikkelsen[5], D. Miller[1], R. Mumgaard[1], R. Murray[1], R. Ochoukov[1], G. Olynyk[1], D. Pace[6], S. Park[1], R. Parker[1], Y. Podpaly[12], M. Porkolab[1], M. Preynas[14], I. Pusztai[1], M. Reinke[1], J. Rice[1], W. Rowan[4], S. Scott[5], S. Shiraiwa[1], J. Sierchio[1], P. Snyder[6], B. Sorbom[1], V. Soukhanovskii[7], J. Stillerman[1], L. Sugiyama[1], C. Sung[1], D. Terry[1], J. Terry[1], C. Theiler[1], N. Tsujii[1], R. Vieira[1], J. Walk[1], G. Wallace[1], A. White[1], D. Whyte[1], J. Wilson[5], S. Wolfe[1], K. Woller[1], G. Wright[1], J. Wright[1], S. Wukitch[1], G. Wurden[13], P. Xu[1], C. Yang[9] and S. Zweben[5]

[1] Massachusetts Institute of Technology, Cambridge, MA, 02139, USA
[2] University of Wisconsin, Madison, 53706, USA
[3] University of California, Los Angeles, 90095, USA
[4] University of Texas, Austin, TX, 78712, USA
[5] Princeton Plasma Physics Laboratory, Princeton, NJ, 08543, USA
[6] General Atomics, San Diego, 94121, USA
[7] Lawrence Livermore Laboratory, CA, 94550, USA
[8] University of Tromsø, Tromso, Norway
[9] Hefei Institute for Plasma Physics, Hefei 230031, Anhui, China
[10] University of California, San Diego, 92903, USA
[11] CompX Corporation, Del Mar, CA, 92014, USA
[12] National Institute of Standards and Technology, Gaithersburg, MD, 20899, USA
[13] Los Alamos National Laboratory, NM, 87544, USA
[14] CEA, IRFM, 13115, Saint Paul lez Durance, France

E-mail: g@psfc.mit.edu

Received 26 October 2012, accepted for publication 30 January 2013
Published 26 September 2013
Online at stacks.iop.org/NF/53/104004

Abstract
Recent research on the Alcator C-Mod tokamak has focused on a range of scientific issues with particular emphasis on ITER needs and on detailed comparisons between experimental measurements and predictive models. Research on ICRF (ion cyclotron range of frequencies) heating emphasized the origins and mitigation of metallic impurities while work on lower hybrid current drive experiments have focused on linear and nonlinear wave interactions that limit efficiency at high densities in regimes with low single pass absorption. Experiments in core turbulence and transport focused on quantitative, multi-field comparisons between nonlinear gyro-kinetics simulations and experimental measurements of profiles, fluxes and fluctuations. Experiments into self-generated rotation observed spontaneous flow reversal at a critical density identical to the transition density between linear ohmic confinement and saturated ohmic confinement regimes. H-mode studies have measured pedestal widths consistent with kinetic-ballooning-mode-like instabilities, while the pedestal heights quantitatively match the EPED code predictions. Experiments with I-mode have increased the operating window for this promising edge-localized-mode-free regime.

Extrapolation of I-mode to ITER suggests that the fusion gain $Q \sim 10$ could be possible in ITER. Investigations into the physics and scaling of the power exhaust channel width in attached enhanced D-alpha H-mode and L-mode plasma showed a direct connection between the midplane pressure-folding length and the outer divertor target footprint. The width was found to scale inversely with I_P, while being independent of conducted power, B_T or q_{95} and insensitive to the scrape-off layer connection length—a behaviour that suggests critical-gradient physics sets both pressure and heat-flux profiles.

(Some figures may appear in colour only in the online journal)

1. Introduction

Alcator C-Mod is a compact ($R = 0.67$ m, $a = 0.22$ m), high-field (8 T) diverted tokamak. Auxiliary power is solely from RF, with 6 MW coupled in the ion cyclotron range of frequencies (ICRF at 50–80 MHz) and 1 MW coupled at lower hybrid (LH) frequencies (4.6 GHz). ICRF provides efficient heating over a wide range of plasma conditions. The principal heating regimes used on C-Mod are 1st and 2nd harmonic hydrogen minority in deuterium, and various mode conversion schemes. It is noteworthy that C-Mod can run at the same magnetic field, plasma density and RF frequencies as ITER, thereby testing RF scenarios with the same cold-plasma dielectric tensor and thus the same RF wave physics as ITER. Core studies feature heating and current drive methods without particle or momentum sources. Plasma-facing components are made of high-Z metals, molybdenum and tungsten, which are of interest for ITER and for fusion reactors because of their superior properties relative to erosion, tritium co-deposition and power handling when compared to carbon based materials. For edge studies, the magnetic field, plasma density ($\langle n_e \rangle = (0.2\text{–}5.0) \times 10^{20}$), parallel heat flux ($q_\parallel > 1\,\mathrm{GW\,m^{-2}}$) and neutral opacity are in the range prototypical of a reactor. Recent research on the Alcator C-Mod tokamak has covered a broad range of scientific issues with particular emphasis on ITER needs and on detailed comparisons between experimental measurements and predictive models.

2. RF actuators

2.1. ICRF heating

C-Mod has demonstrated excellent H-mode confinement with high-power ICRF heating after boronization, but the coating must be renewed at regular intervals. In general, wall coatings of boron (or other low-Z materials like beryllium) can mitigate the effects of impurity influx on machines with short pulse or low power, but this solution does not extrapolate to a steady-state reactor regime. Production of high-Z metallic impurities through generation of high-voltage RF sheaths is a critical issue for machines with metal walls like ITER. Thus, research on ICRF heating has focused on understanding and mitigating the mechanisms for impurity generation.

New probe diagnostics show that ICRF heating has complex interactions with the scrape-off layer (SOL) and produces sheath voltages greater than 100 V consistent with molybdenum sputtering from ions accelerated through the potential [1]. This can be compared to OH plasmas where potentials on the order of 10 V are measured. The effect is seen on surfaces local to, and remote from, the ICRF antennas. On field lines that map to the antenna, measured potentials are consistent with a slow-wave rectification mechanism [2]. At the same time, ICRF strongly modifies the phase velocities of the far-SOL broadband turbulence measured far from the antenna near-field [3]. An assumption that the change in phase velocity is due to $E \times B$ motion yields values for E_r in the far SOL as large as $40\,\mathrm{kV\,m^{-1}}$ and associated electric potentials as large as 400 V. The implied E_r scales with the square root of P_{RF} and is thus proportional to the E_{RF} amplitude. The scale length for the SOL modification, $\sim$1 cm, is about five times the skin depth, suggesting a nonlinear plasma response. The response is seen far from the ICRF antenna, on field lines where $E_\parallel$ does not integrate to zero. These electric field structures may play a role in both the source and transport of impurities, but as of now, the relative importance of these two effects is uncertain.

Building on these results, 3D finite element antenna modelling predicted significantly reduced parallel electric RF fields, responsible for the RF-induced potential sheath, if the antenna current straps were aligned perpendicular to the total magnetic field [4]. This antenna configuration should be contrasted with conventional antennas on which the straps are in the poloidal plane, even if their Faraday screens are field-aligned. To test this model, a novel field-aligned antenna has been recently constructed and installed [5]. Initial results are promising; in addition to sharply reduced high-Z impurity production the antenna achieved power densities up to $9\,\mathrm{MW\,m^{-2}}$, similar to required ITER values, and was more resilient to load variations. Figure 1 compares the metallic impurity content in the plasma, between the new and older antenna configurations under similar conditions. Visible spectroscopy and imaging suggest reduced erosion sources of molybdenum near mid-plane limiters during operation of the field aligned antenna compared with the non-field aligned antennas. Despite the success of this technology, differences between the experiment and antenna modelling were found. Although impurity sources were dramatically reduced, the measured RF-induced potentials in the far SOL were actually larger than those of the antenna it replaced [6]. And while the model predicted lower integrated $E_\parallel$ for monopole phasing, this mode of operation had higher impurity content and higher potentials.

Experiments were also carried out to test full-wave models of ICRF propagation and heating in the plasma. ICRF simulations with the RF and Fokker–Planck codes TORIC [7], AORSA [8] and CQL3D [9] compared predictions of fast ion spectra to measurements made with a compact neutral analyser [10]. Generally there was good agreement with the equilibrium fast ion population and its scaling with I_P and P_{ICRF}. Figure 2 shows the comparison between measured and simulated fast ion spectra [11]. At the same time, however, there was disagreement on the transient formation and decay of

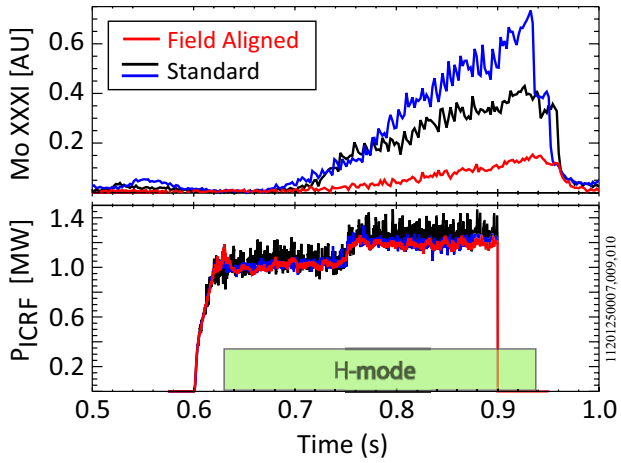

Figure 1. High-Z impurity sources are dramatically reduced with the new field-aligned ICRF antenna. The top plot shows the intensity of radiation from molybdenum in the plasma core for the different antenna configurations. While the bottom plot shows the RF power.

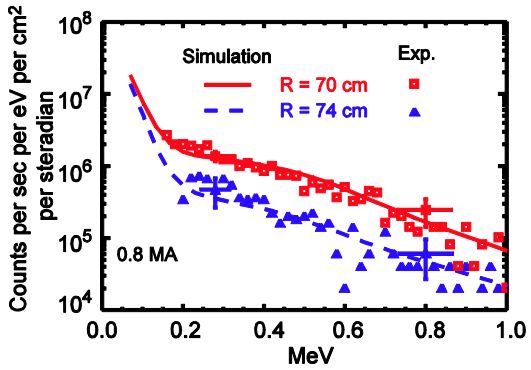

Figure 2. Measured fast-ion spectra (solid points) are in good agreement with simulations (lines) with the full-wave, all-orders ICRF code AORSA [11]. Reproduced with permission from [11]. © 2011 American Institute of Physics.

the fast ion tail, with the experimental measurements evolving on a considerably faster time scale. The physics behind this difference is under investigation. Using a PCI diagnostic [12], measurements of ICRF wave intensity in the plasma were compared to simulations from AORSA with output processed as a synthetic diagnostic. As seen in figure 3, reasonable agreement was found in the minority heating regime, however fundamental disagreement was found for mode conversion heating. In this case the code over-predicted the wave intensity by as much as a factor of 50 [13]. This may be the result of nonlinear effects, such as parametric decay (parametric decay instability—PDI), which have not been studied extensively in this regime. Experiments to increase mode-conversion flow drive beyond levels previously reported [14] were limited by development of neoclassical tearing modes [15]. The onset criteria was similar in terms of β_N/ρ^* and collisionality to that previously reported by DIII-D and AUG [16].

2.2. *Lower hybrid current drive (LHCD)*

Through experiments and modelling, coupling studies have elucidated the role of the ponderomotive effect on LH coupling via a reduction in plasma density in front of the launcher [17]. ICRF waves from nearby antennas can have a similar

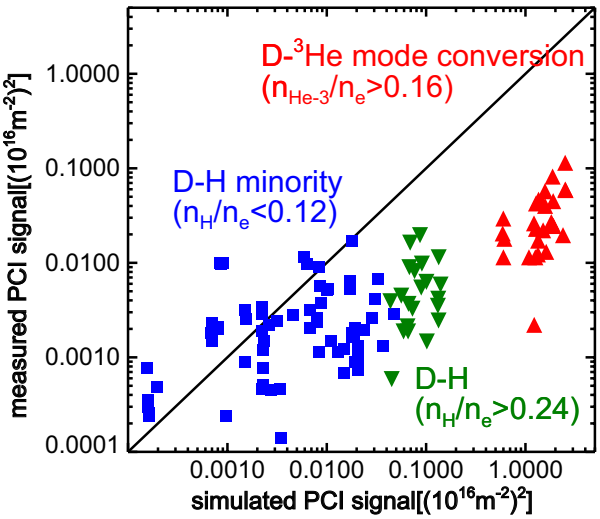

Figure 3. ICRF wave intensity, measured in the plasma with a phase contrast imaging diagnostic is compared to simulations. While rough agreement is obtained for minority heating, there is a substantial over-prediction for mode-conversion scenarios [13]. Reproduced with permission from [13]. © 2012 American Institute of Physics.

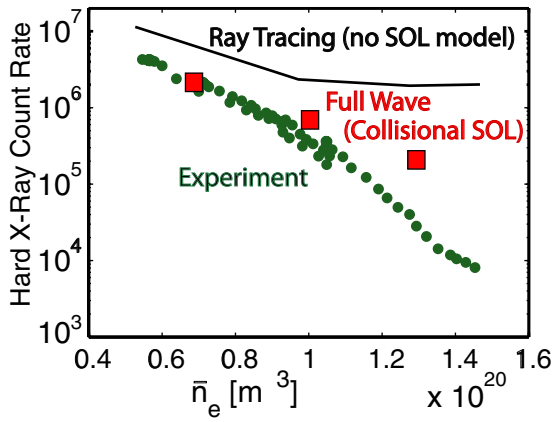

Figure 4. Hard x-ray intensity, which is a measure of the fast-electron population created by LHCD, is plotted versus density and is seen to drop well below the predictions of a simple ray tracing calculation, made without inclusion of any parasitic processes occurring in the edge plasma. Some, but not all of these effects can be captured by more complete modelling.

effect, lowering the density and increasing reflections [18]. LHCD experiments have demonstrated efficient current drive at moderate densities, achieving 100% non-inductive operation in the density range $0.5 \times 10^{20}\,\mathrm{m}^{-3}$, close to the projected conditions for ITER steady-state operation. Off-axis current drive enabled creation of an electron internal transport barrier (ITB), likely through modification of magnetic shear [19]. However, at high densities, $n_e > 10^{20}$, but well below the limit for wave accessibility, LHCD efficiency drops faster than expected [20]. This effect has been studied with ray tracing (GENRAY [21]/CQL3D) and full-wave (LHEAF) simulations [22]. Figure 4 compares experimental measurements of the hard x-rays produced by fast electrons and the expectations of a ray tracing calculation that neglects parasitic processes in the plasma edge. A number of mechanisms have been identified

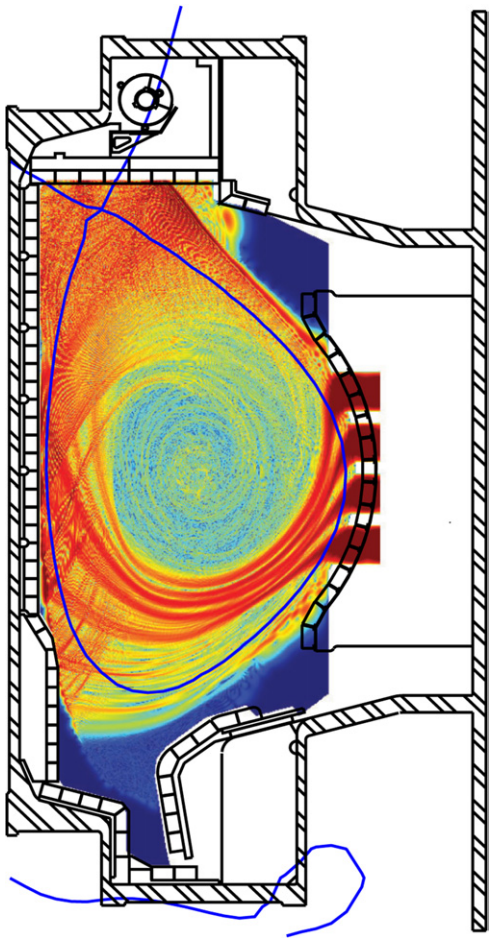

Figure 5. A map of LH wave intensity from a full-wave simulation for a high-density ($>10^{20}$ m^{-3}) plasma. A large fraction of wave energy propagates in the plasma edge and SOL.

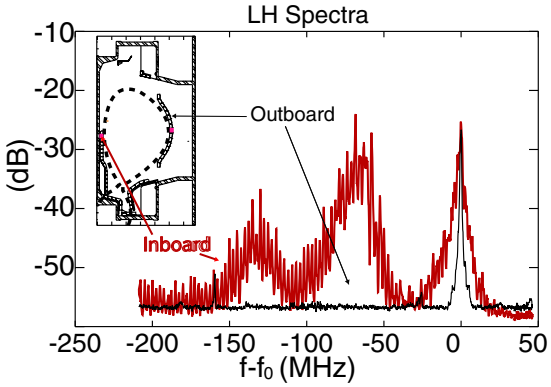

Figure 6. Probe measurements of the LH wave power spectra find evidence of nonlinear processes (likely PDI) that contribute to the loss of LHCD efficiency at high density.

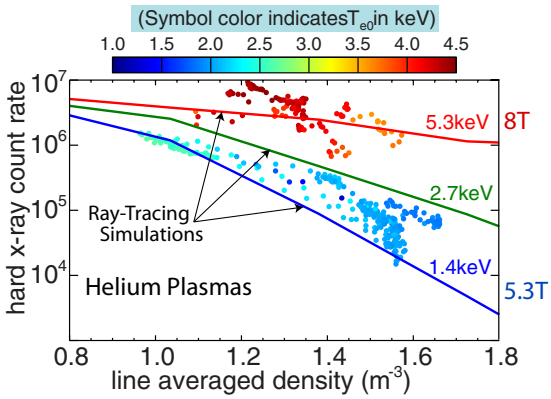

Figure 7. The loss of LHCD efficiency at high density, as seen in the hard x-ray emission, is recovered under conditions with good single-pass absorption, in this case at high electron temperatures.

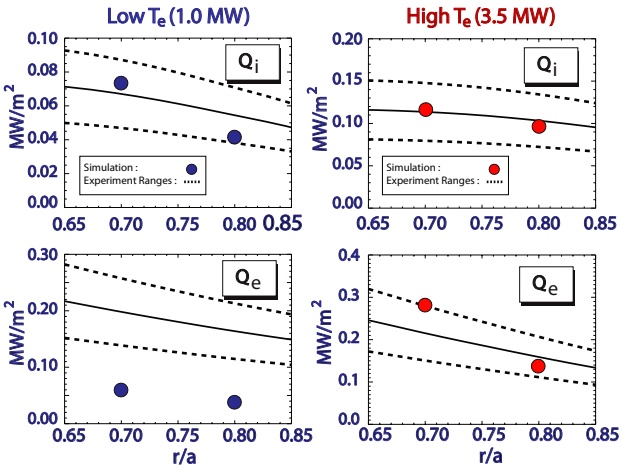

Figure 8. Gyro-kinetic predictions (solid symbols) of ion heat flux are plotted at different radii and do not find the 'shortfall' compared to experimental heat flux (lines) previously reported on other devices [17–19]. In low power discharges, there is an under-prediction for electron heat flux, that is not observed at higher power.

so far—all connected to low single-pass absorption—including spectral broadening due to full-wave effects and plasma density fluctuations, nonlinear interactions such as the PDI, collisional damping and loss of fast electrons in the plasma scrape-off layer (SOL) [23]. Visible spectroscopy and imaging reveal local limiter heating and enhanced erosion in areas with magnetic field-line mapping to the LH antenna horns [24]. (Direct scattering by edge fluctuations is apparently unimportant [25].) Figure 5 is the predicted wave amplitude from a full-wave calculation for a high-density plasma showing that a large fraction of the wave energy propagates in the plasma edge and SOL at high densities. Figure 6 shows evidence of PDI in measurements of the RF frequency spectra taken at the high-field side midplane. Modelling suggests that low single-pass absorption enhances the wave amplitude in the regions where conditions allow the PDI to grow—consistent with a model by Takase [26]. According to these models, running with higher single-pass damping (as in ITER) could mitigate all of the identified mechanisms. Experiments at higher plasma temperature, which increases the damping and reduce edge effects, do in fact demonstrate LHCD efficiencies close to the accessibility limit (see figure 7). Based on these results, improved geometry for the LH launcher is being pursued and extensive modelling and design are underway for an off-midplane launcher [24, 27]. This design reduces reflected power via a toroidal bi-junction while retaining control of the $n_{\|}$ spectrum. Velocity space synergy with the midplane launcher is predicted to maximize driven current at ITER relevant densities.

3. Core turbulence and transport

3.1. Multi-channel transport studies across the electron–ion boundary

A series of experiments has investigated multi-channel transport phenomena across the ITG/TEM boundary. The under-prediction of transport by nonlinear gyro-kinetic simulations compared to experimental measurement, in the outer regions of the plasma, $r/a \sim 0.75$–0.85, is the subject of intense interest [28–30]. By comparison and as shown in figure 8, GYRO [31] simulations on C-Mod show a moderate shortfall in low-power, low-temperature L-modes and only in the electron channel [32]—unlike DIII-D which observed the effect in the ion channel as well [28]. At higher power in I-mode, the shortfall disappeared in C-Mod, consistent perhaps with the hypothesis that the shortfall occurs when the gyro-Bohm normalized power is small [33]. At the same time, levels of T_e and n_e fluctuations in these experiments drop following a transition from L- to I-mode (figure 9). Both experiment and nonlinear simulation show an increase in fluctuation amplitude with radius, with T_e fluctuations generally increasing in response to stronger TEM drive. A change in the rotation profile from peaked to hollow was observed in a downward density scan. Contrary to some expectations, there was apparently no correlation of the appearance of this rotation phenomenon to the linear calculation of the ITG/TEM boundary. However, nonlinear gyro-kinetic simulations did find a change in direction of the momentum flux corresponding to the profile differences found between the two values of density studied in the experiment. Additional work in modelling momentum transport in these plasmas is ongoing.

3.2. Impurity transport validation studies of the gyro-kinetic model

Studies of impurity particle transport were carried out using laser blow-off (LBO) to create a well-defined calcium impurity source [34]. Spatially and temporally resolved soft x-ray spectra of Ca^{18+} were analysed to measure the evolution of impurity-line brightness profiles and a single chord VUV measurement of Ca^{17+} helped constrain calculations of the charge-state balance. The STRAHL code was then run in an interative loop to determine experimental diffusivity and convective velocities along with experimental uncertainties [35]. Using the GYRO code and detailed uncertainty and sensitivity analysis, it was possible for the first time to demonstrate quantitative, simultaneous agreement between nonlinear gyrokinetic calculations and experimental observations for impurity diffusion, convection and ion heat flux [36] (see figure 10). Electron heat flux is under-predicted and extension of the simulations to include short wavelength modes, up to $k\rho_s$ of 3, does not increase the predictions significantly. Work is ongoing to simulate ETG turbulence, at still higher values of k, and to look for the effects of micro-tearing modes. In related work, nonlinear simulations of peaked main-ion density profiles at low collisionality matched the experimental 'null-flux' observation, with higher k turbulence responsible for the inward convection. Investigations of parallel impurity

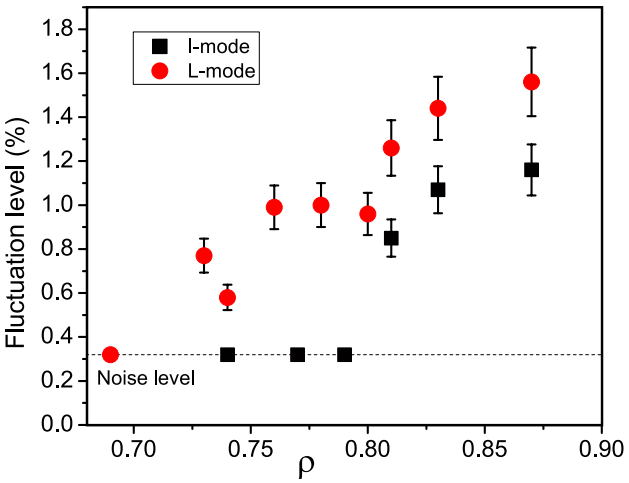

Figure 9. Electron temperature fluctuations have been measured with a correlation ECE diagnostic. These show a drop in fluctuations following an L- to I-mode transition and a monotonic increase with radius. Both trends are consistent with gyro-kinetic simulations.

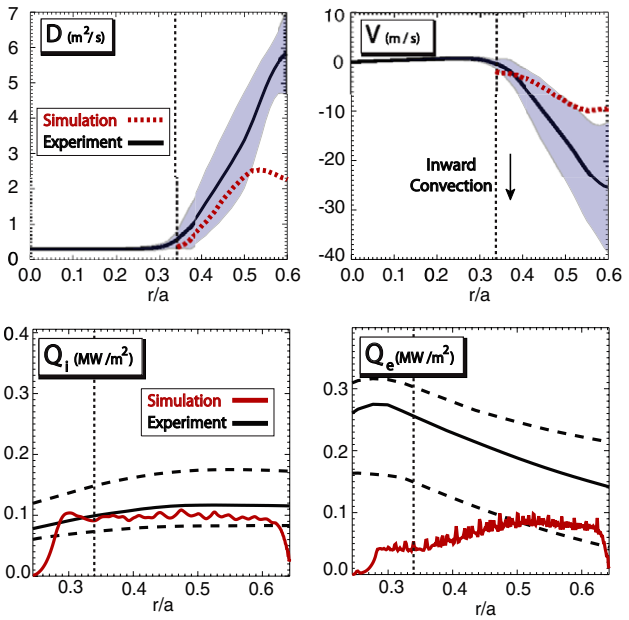

Figure 10. Simulations with GYRO can simultaneously match impurity particle diffusivity, convective velocity and ion energy flux. Electron energy transport is not matched, perhaps due to the lack of full electron dynamics and electron-scale modes in this simulation.

transport found that the observed poloidal asymmetries in impurity density could be explained by a model which included effects from plasma rotation and electric field build-up from non-uniform poloidal distribution of ICRF-created fast ions [37].

3.3. Transport studies across the linear ohmic confinement/saturated ohmic confinement boundary

Experiments into self-generated rotation in torque-free C-Mod discharges found an unexpected connection between momentum and energy transport. Spontaneous flow reversal was observed at a q-dependent critical density and found to be identical to the transition density between linear ohmic

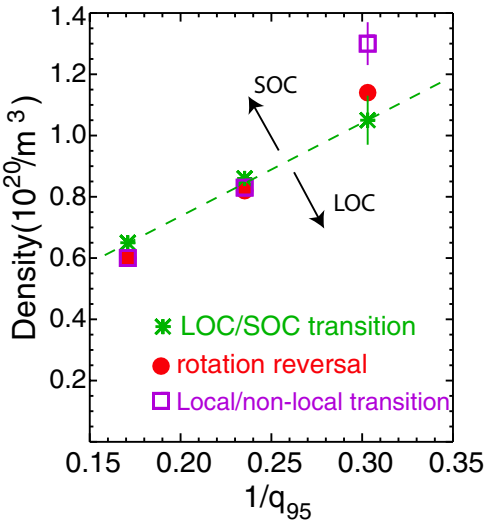

Figure 11. The transition between LOC and SOC confinement, core rotation reversal and the transition between 'local' and 'non-local' transient transport all occur at the same, q-dependent critical density.

confinement (LOC) and saturated ohmic confinement (SOC) [38]. Power balance calculations clearly show that electron energy transport dominates in the LOC with ion transport increasing sharply in the SOC. Flow reversal at the boundary between the two regimes occurred in the plasma core, inward of the $q = 3/2$ surface and was accompanied by a marked drop in density fluctuations ($k\rho_s \approx 0.15$–0.7) and electron temperature fluctuations ($k\rho_s \leqslant 0.3$) as the density was raised [39]. The sharp drop in T_e fluctuations is qualitatively consistent with linear gyrokinetic calculations suggesting a transition from TEM to ITG turbulence as the density rises. Using perturbative injection of calcium with the LBO system, transient analysis of heat flux showed that a transition between non-local and local transport also occurs at precisely the same LOC/SOC boundary [40], consistent with inferences from earlier studies [41]. While the physical interpretation of these terms is a matter of some controversy, in this context we use phenomenological definitions where a 'local' response refers to a slow drop (on the order of a confinement time) in temperature in the plasma core following the prompt edge cooling by the injection of impurities. The 'non-local' response is a prompt temperature rise (much shorter than a confinement time) in the core following the edge cooling. Figure 11 compares the q-dependent critical density for these phenomena. Perhaps the most surprising aspect of these observations is the sharp boundary between the two regimes. There is currently no obvious theoretical framework that would explain a sudden rather than gradual transition between TEM and ITG dominated turbulence. Nonlinear gyrokinetic modelling of the LOC regime suggests that the observed decrease in ion heat flux may be due to ion dilution, with observed fluctuations measured by PCI in agreement with GYRO simulations. The effect is observed using measured Z_{EFF} and assuming the average impurity Z to be 8. In this case ion dilution is computed to be as high as 30% and TEM dominates over ITG. The agreement is limited to a radial range of $0.6 < r/a < 0.8$.

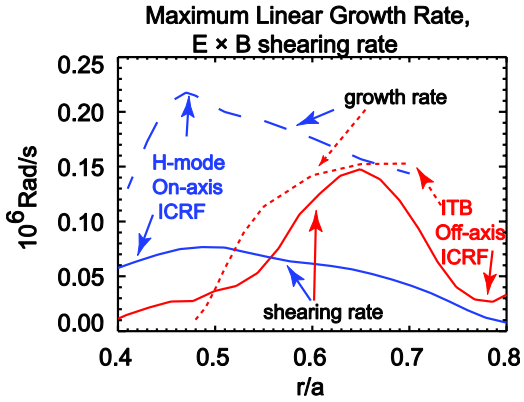

Figure 12. Shear in self-generated rotation increases with off-axis ICRF heating, attaining values close to the simulated linear growth rate of ITG instabilities. This may be the first example of an ITB created by self-generated equilibrium flows [42]. Reproduced with permission from [42]. © 2012 American Institute of Physics.

3.4. Internal transport barriers

It was shown for the first time on C-Mod that ITBs could be created with the aid of self-generated $E \times B$ shear flow [42]. These were produced by off-axis heating which also aided barrier formation by reducing the ion temperature gradient (R/L_{T_i} drops from 5 to 3) and thus the drive for ITG turbulence. Linear analysis with gs2 [43] and GYRO shows $E \times B$ shearing reaches the ITG growth rate as the barrier forms (figure 12) contrasting with a standard H-mode where the linear growth rates are always well above the shearing rate. Nonlinear GYRO simulations found a clear effect of the self-generated flow in reducing turbulent heat transport—the drop in ion temperature gradient alone would not be sufficient to produce a barrier. A new series of ITB experiments used modulated ICRF heating to study TEM induced particle transport which decoupled core and edge density fluctuations for comparison to gs2 simulations [44] and validated a nonlinear upshift predicted for the turbulence onset [45]. The nonlinear TEM threshold appears to clamp the density gradient in modulated heating experiments in C-Mod ITBs as shown in figure 13 where the density gradient is seen to rise well above the much lower linear stability threshold. Gyrokinetic simulations show the nonlinear upshift of the TEM critical density gradient is associated with long-lived zonal flow dominated states, increasing strongly with collisionality [46]. The resulting temperature dependence allows external RF heating to control TEM turbulent transport.

4. Pedestal and edge barrier physics

H-mode studies have focused on the pedestal structure and relaxation mechanisms. It is essential to develop predictive models for the threshold, that is to predict when a plasma will be in H-mode, and for the pedestal height—because of the strong connection to core performance. The I-mode is an interesting and potentially important new regime that provides high-performance without large edge-localized modes (ELMs) [47, 48].

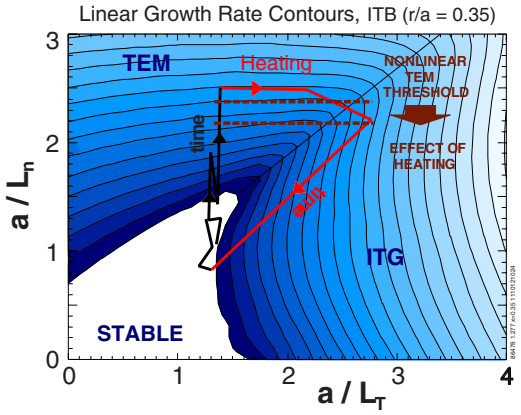

Figure 13. The experimental trajectory of an ITB with modulated on-axis heating is overlaid onto the contours of the computed linear gyro-kinetic growth rates in plane of the normalized temperature and density gradients. It is seen that the experimental profiles are limited by the nonlinear threshold, which is upshifted significantly from the linear threshold.

4.1. Pedestal and H-mode

In ELMy H-modes the measured pedestal width is consistent with kinetic-ballooning-mode(KBM)-like instabilities with weak β_P scaling, while, as seen in figure 14, the pedestal heights quantitatively match the predictions [49, 50] from the EPED model [51] which uses limits imposed by the linear stability of kinetic-ballooning and global peeling–ballooning modes. For multi-machine studies of the pedestal structure, C-Mod extends the pressure range by a factor of 3. Studies of the L–H transition have focused on characterizing the density at which the power threshold is minimized and on the effects of plasma geometry. It is clear from figure 15 that the simple power law scaling does not capture the 'U-shaped' density dependence which shows a sharp increase at both lower and higher density [52]. The local threshold seems to be characterized by a critical temperature in the higher density branch and by a critical pressure at low density. The global scaling is likely capturing multi-machine dependence of U-shaped data clusters, probably accounting for some of the large scatter found in the scaled data. A more reliable approach may be to first determine the scaling of the density at the minimum of the power threshold and then carefully characterize the threshold scaling around that operating point. In scans of B_T and I_P at fixed shape on C-Mod, the minimum-power density was found to scale roughly linearly with B_T and does not depend on I_P or q [53]. Multi-machine studies [52] suggest an inverse size scaling leading to a leading dependence roughly like B/R. With shape and q in a narrow range, this is indistinguishable from a scaling with the tokomak density limit [54], as suggested in [52], and predicts an achievable threshold power for ITER, though the threshold would likely increase with density, from that point, faster than linearly. The minimum in threshold power appears to be correlated with the transition between sheath limited and conduction limited divertor regimes. A dramatic drop in the threshold power was observed as the plasma strike-point was moved from C-Mod's inclined plate divertor into the open 'slot'. The drop, which could be by as much as 50%, was correlated to an increase in the length of the outer divertor leg. These observations prompted comparisons with the FM3 (Fundamenski–Militello–Moulton–McDonald) model [55] which recovers the observed B_T and density dependences, and provides quantitative agreement, though requiring empirical calibration factors from the data set. Ultimately a predictive model will require a more first-principles approach to the threshold and to the edge plasma profiles obtained in L-mode. The threshold L-mode profiles are roughly consistent with the Rogers–Drake–Zeiler (RDZ) model [56] that derived a collisionality dependent critical pressure gradient for the transition.

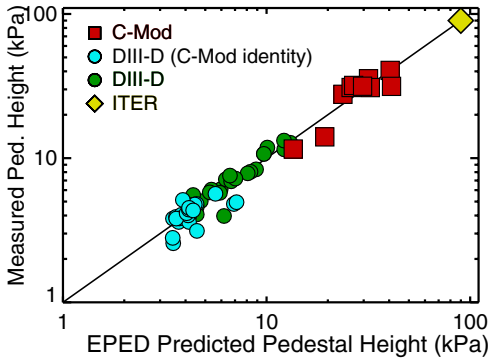

Figure 14. Pedestal height, measured on C-Mod, are well predicted by the EPED model. The C-Mod data extends the database from DIII-D by a factor of three, more closely approaching the values required for ITER.

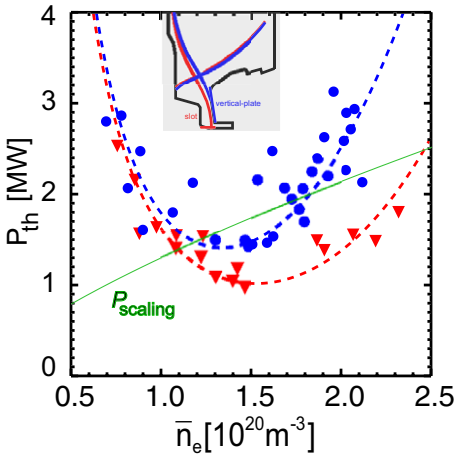

Figure 15. The L–H power threshold is not well characterized in detail by the global power law scaling, however the scaling line does capture the centroid of the data. Sensitivity to magnetic topology suggests an important role for divertor physics in setting the power scaling [53]. Reproduced with permission from [53]. © IAEA.

4.2. I-mode

Standard H-modes have the good energy confinement required to extrapolate to fusion burn, but are accompanied by significant drawbacks. The edge barrier typically rises to an MHD stability limit causing ELMs that extrapolate to unacceptable transient heat loads in reactors. Even with ELMs, impurity confinement is much higher than in L-mode and can lead to a degradation in performance in machines with high-Z walls. Thus a high-performance regime with reduced particle

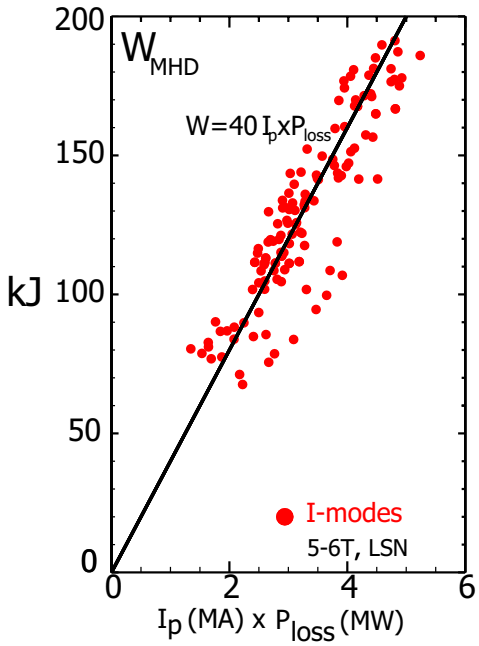

Figure 16. Stored energy in I-modes, created by strong heating in configurations with the ion ∀B drift away from the x-point do not show the power degradation typical of L- or H-mode.

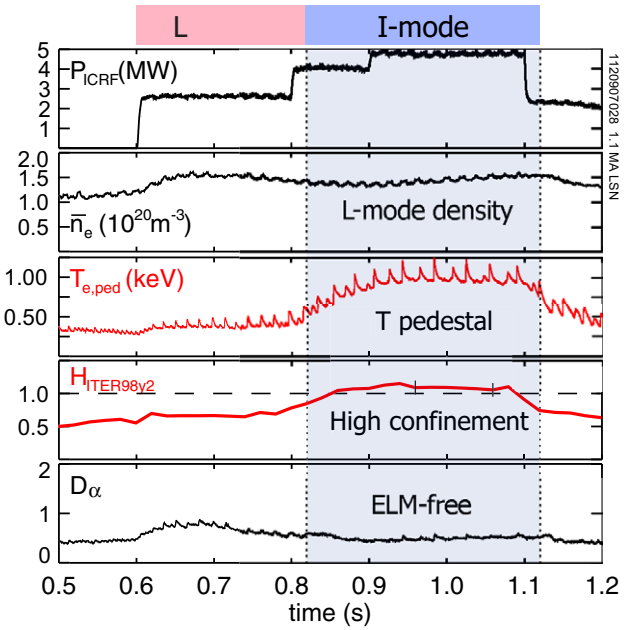

Figure 17. Steady I-mode operation is seen to be achieved at high-performance, $H_{98} \sim 1$, without ELMs or increase in particle or impurity confinement.

confinement and without large ELMs is actively sought. Experiments with I-mode on Alcator C-Mod have increased the operating window for this promising ELM-free regime [48]. I-mode discharges, which are created by strong heating in a configuration with the ion-drift in the 'unfavourable' direction (that is away from a single-null divertor), have a large T_e pedestal and H-mode-like energy confinement simultaneously with L-mode-like particle transport and no density pedestal. H_{98} is 1 ± 0.2. Moreover, as seen in figure 16, over the power range investigated, no significant power degradation in confinement was observed. It is critical to distinguish between I-mode, a steady-state regime with a novel form of edge barrier and the similar sounding 'I-phase', a limit cycle behaviour between conventional L- and H-modes. The steady nature of I-mode can be seen in figure 17, where the I-mode is maintained for seven energy confinement times, limited so far only by external engineering constraints. Impurity confinement is found to be L-mode like, making I-mode compatible with high-Z walls and low-Z impurity puffing, the latter being an important tool for reducing power loads to the divertor. I-modes are generally ELM-free and the lack of large ELMs is consistent with calculations using the ELITE code [57], which finds the I-mode pedestal to be MHD stable [50]; instead, the edge particle transport is apparently controlled by a weakly coherent electromagnetic mode. The transition between L- and I-modes, which only involves the energy transport channel, should shed additional light on transport bifurcations in general and the H-mode transition in particular. As discussed below, fluctuations in distinct frequency bands seem to be separately responsible for energy and particle transport. Extrapolation to ITER, using a reasonable set of scaling rules, suggests that $Q \sim 10$ could be possible in an ITER I-mode. Such a scenario would entail entering I-mode at low pedestal density, $\sim 0.4 \times 10^{20}\,\mathrm{m}^{-3}$, and fuelling as the fusion power is increased. This scenario has been demonstrated on C-Mod in experiments where the I-mode density was raised by gas puffing from 1.5×10^{20} to 2×10^{20} in 0.3 s. It is noteworthy that these experiments are already at a substantial fraction of the ITER neutral opacity, providing more confidence in the fueling scenario. Density and size scaling for the L–I threshold are critical to an extrapolation and are the current focus of multi-machine studies under the ITPA.

4.3. Edge barriers and fluctuations

A future challenge will be to extend pedestal structure predictions to discharges with small or no ELMs as required for extrapolation to a reactor. In these cases, nonlinear evolution of the pedestal constrained by small-scale instabilities will be key. Three distinct high-performance ($H_{98} = 1.0 \pm 0.2$), edge-barrier regimes are studied on C-Mod: ELMy and enhanced D-alpha (EDA) H-modes and I-mode. In all three, short wavelength, electromagnetic modes are observed that appear to be important for regulating pedestal transport. At low collisionality and weak shaping, ELMy H-modes are obtained. As discussed above, the maximum pedestal gradient in this regime is well described by MHD stability boundaries. Between ELMs, however, n_e and B_θ fluctuations in the range 250–550 kHz, $\delta f/f \approx 30\%$ and $k \approx 0.6$–$0.7\,\mathrm{cm}^{-1}$ are observed to grow (see figure 18). The mode amplitude is almost extinguished at the ELM crash and recovers as the pressure gradient is re-established. We are investigating whether this is evidence for the kinetic-ballooning mode, which is predicted to regulate pedestal profiles until the peeling–ballooning becomes unstable and leads to an ELM. At higher collisionality, C-Mod runs in EDA H-mode [58]. In this regime, n_e and B_θ fluctuations at 50–150 kHz, $\delta f/f \approx 10\%$ and $k \approx 1.5\,\mathrm{cm}^{-1}$ drive sufficient particle transport to keep

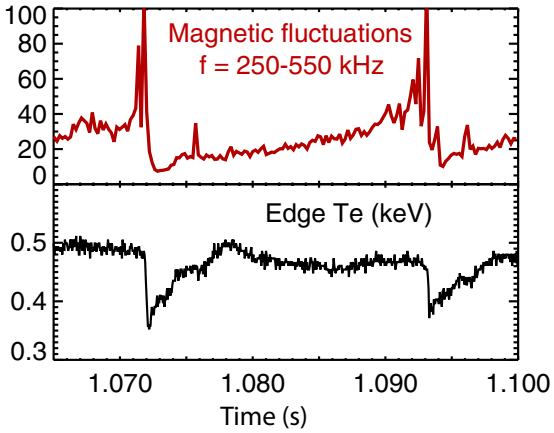

Figure 18. Short wavelength electro-magnetic fluctuations with $k \approx 0.6$–$0.7\,\mathrm{cm}^{-1}$, are observed to increase between ELMs as the pressure gradient recovers. This may be evidence for predicted kinetic-ballooning modes.

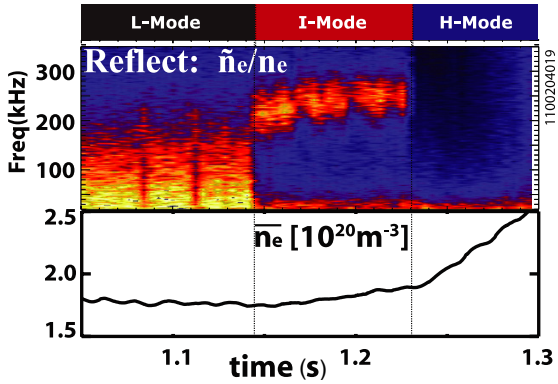

Figure 19. At the L–I transition, density fluctuations below 200 kHz are sharply reduced (top plot) and are replaced (not Doppler shifted) by higher frequency fluctuations that are associated with L-mode like particle transport. The density plot (bottom) shows the clear difference in particle transport for the two regimes.

the pressure profile below the peeling–ballooning boundary [50]. The higher collisionality also reduces bootstrap current and thus the peeling mode drive. Recent measurements observed large (order 1) T_e fluctuations as part of the QC mode, accompanying previously measured fluctuations in n_e, φ and B_θ. ELITE calculations show that these plasmas are ideal MHD stable, as expected for an ELM free pedestal, but the BOUT++ code finds that they are unstable to resistive ballooning, with the pedestal destabilized by collisionality and stabilized for high n modes by diamagnetism [50]. Overall, the BOUT++ results are consistent with the observed experimental scaling for q, m_i and ν^* for EDA operation.

The transition from L- to I-mode is accompanied by a drop in low frequency n_e and B_θ fluctuations, 50–100 kHz. As seen in figure 19, these are usually replaced by a higher frequency, 200–300 kHz, $k_\theta \approx 1.5\,\mathrm{cm}^{-1}$, 'weakly coherent mode' (WCM), seen in the density, temperature and magnetic fluctuations. Measurements of E_r show that this feature is not simply a Doppler shift of the lower frequency fluctuations. The modification of the fluctuation spectrum is associated with the shift from L-mode energy and particle transport to I-mode with its sharply reduced energy transport and L-mode-like particle confinement. In I-mode, the local particle diffusivity increases monotonically with the WCM amplitude [59]. In this regime, $k_\theta \approx 0$ geodesic acoustic modes (GAMs) are found. These are observed via gas-puff imaging as weak density fluctuations, but very strong velocity fluctuations. Bispectral analysis shows these GAMs to be coupled to the WCM [60] with the width of the WCM due in part to the Doppler shift and partly to nonlinear energy redistribution. The relation between the WCM and the somewhat longer wavelength fluctuations seen in low collisionality ELMy discharges between ELMs is not yet clear.

5. Boundary plasmas

5.1. Divertor heat flux

Investigations into the physics and scaling of the heat-flux footprint at the outer divertor target plate were aided by an extensive set of new diagnostics [61]. The conclusions of these studies of attached EDA H-modes and ohmic L-modes were that the midplane pressure profile maps to the divertor and, due to the relatively flat T_e profile at the divertor target, essentially determines the width of the footprint. Direct measurements of sheath heat transmission coefficients show agreement with theoretical values [62] and have been used to delineate regimes in which Langmuir probe measurements can be trusted [63]. Narrow widths were associated with steeper pedestals and higher global energy confinement [61]. The width was found to be independent of conducted power, B_T or q_{95} and insensitive to the SOL connection length. All of this points to the dominance of marginal stability in turbulent perpendicular transport. As at the midplane, I_P (or B_P) is the strongest control parameter. The observation that the pressure profile across the separatrix sets the divertor heat-flux footprint combined with constraints on the H-mode pedestal allows extrapolations to be made for the ITER power channel width [64]. This method yields ITER heat-flux footprint widths, λ_q, the perpendicular scale length for parallel heat exhaust mapped to the midplane, in the range 10–30 mm, which is contrary to recent projections of $\lambda_q \sim 1$ mm, based on a multi-machine regression analysis [65]. The heat-flux profiles are asymmetric, generally with a longer fall-off into the SOL than into the private flux zone (PFZ). By fitting to an asymmetric function, the dependence of each part can be investigated. What is found is that the overall scaling dependences are dominated by changes in the SOL half-width rather than the PFZ width, which does not depend strongly on I_P or stored energy [66]. At the same time, heat flux can be reduced to about 10% of the total input power via impurity seeding, while maintaining good H-mode energy confinement even with power close to the threshold, meeting ITER scenario targets [67].

5.2. Blob dynamics

Large intermittent structures dominate the far-SOL and plasma–wall interactions away from the divertor strikepoint. The structures, typically called 'blobs' or 'bursts', contain most of the plasma in the far-SOL and have density and temperature that are much higher than the surrounding plasma. The creation and motion of the blobs is associated with potential structures arising from uncancelled particle drifts. New measurements

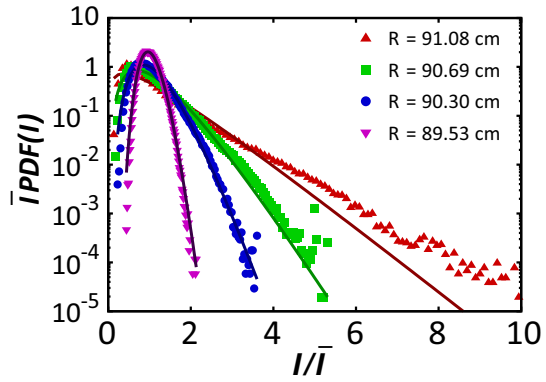

Figure 20. The PDF for 'blob' amplitude at different radii for $n/n_G - 0.2$. The separatrix is at 89.3 cm. This plot shows the exponential distribution of intensities over five orders of magnitude and demonstrates the increasing intermittency seen farther out in the SOL.

using the gas-puff imaging diagnostics [68] allow collection of data with an unprecedented dynamic range in event amplitude and duration [69]. Figure 20 shows the intensity distribution of blobs measured at different radial locations in the SOL. These show a standard result—a Gaussian distribution near the separatrix and a distribution that becomes increasingly asymmetric as one moves further out in the SOL. Note that these new data span five orders of magnitude. Using the measurements as a guide, a statistical model was developed which can match the SOL fluctuation data over this enormous range [70]. The model has the following elements: constant burst duration and shape, with a fast rise and slow decay, burst amplitudes distributed exponentially and waiting times (time between bursts) distributed exponentially. These statistics suggest random, uncorrelated processes underlie the fluctuation dynamics. Moreover, three numbers, the amplitude, birth duration and the average waiting time, completely characterize the process [71]. This may provide a powerful tool for validating edge turbulence models which should reproduce these three quantities.

5.3. Effects on pedestal and fluctuations by LH waves

Modest power levels of LH can have a substantial impact on the pedestal profiles and overall plasma performance, even in cases where the LH waves cannot access the core plasma [72]. In typical experiments, LH power, $n_\parallel = 1.9$, on the order of 0.5 MW is launched into established H-modes, with ICRF power in the range 2–4 MW and plasma densities above $3 \times 10^{20}\,\mathrm{m}^3$. This is well above the LH accessibility limit and three times the density where efficient current drive has been achieved. Ray tracing codes find that the waves barely skim through the pedestal. Nonetheless, pedestal profiles are strongly modified, with pedestal temperature increasing, as shown in figure 21(*a*) and pedestal density dropping. Stored energy increases by 30–40%. If confinement were fixed, this same increase would require roughly doubling the input power. Accompanying the change in profiles and energy content, edge and SOL fluctuations drop by about an order of magnitude, as shown in figure 21(*b*). There is also a change observed in the QC mode frequency and amplitude. While the nature of the LH–pedestal interaction is not understood at this point, it may provide a novel mechanism for pedestal and confinement control.

6. Plasma–wall interactions

6.1. Tungsten nanostructures

Under suitable conditions, the growth of tungsten nanostructures ('fuzz') has been observed in plasma–wall test stands [73]. This observation has raised concerns about erosion and dust generation in reactor environments. The working hypothesis for their formation is that the structures, which consist of small filaments, are extruded by helium bubbles captured in the metal substrate. An open question was whether these same processes could occur in the actual operating environment of a confinement experiment and whether other plasma–wall processes would destroy the structures before they could grow to a significant size. On C-Mod, a careful experiment was performed to raise a tungsten sample to the correct surface temperature, about 2000 K, and expose it to L-mode helium plasmas for a sufficient time to match the fluxes and fluences employed on the Pilot-PSI test stand [73]. This resulted in structures with nearly identical morphology and growth rates (tendril diameter ∼100 nm and growth rate ∼600 nm in 13 s of exposure at temperature—see figure 22) [74, 75]. Helium concentrations in the fuzz layers were measured at 1–4%, which is well above natural solubility of helium in tungsten, but below the values expected for pressure-driven growth. The interpretation of this observation with respect to the physical mechanism for tendril growth is unclear. Erosion rates from sputtering of the tungsten sample were well below the fuzz growth rate however nearby molybdenum surfaces operating at lower temperatures were predicted to have faster sputtering than growth. As predicted, these surfaces did not show evidence of surface nano-structures. Overall, we conclude that the tokamak environment has little or no impact on tungsten fuzz growth when compared to linear plasma devices. This provides confidence that key growth parameters identified in linear devices can be used to predict surface behaviour in future devices. This does not mean that future experiments on confinement experiments are unimportant. A number of critical questions must still be answered. Largely unknown are the effects of the fuzz on tokamak operations including wall recycling, fuel retention, erosion and dust production. We must also clarify the effects on fuzz growth of large ELMs, impurity seeding and mixed wall materials.

6.2. In situ measurement of plasma–wall interactions

A 1 MeV deuteron ion beam was installed to provide the first *in situ* measurements of plasma–wall interactions [76]. Figure 23(*a*) shows the geometry of the beam relative to the C-Mod tokamak. The beam can be steered by small currents in the toroidal and poloidal field coils to cover a representative set of first wall tiles. The measurements can be made rapidly and without removing samples from the vessel. The diagnostic exploits specific nuclear reactions to measure particular plasma–wall processes. For example,

$\mathrm{D} + \mathrm{B}^{11} \Rightarrow \mathrm{P} + \mathrm{B}^{12} + \gamma$ (to measure the thickness of boron coating),

$\mathrm{D} + \mathrm{D} \Rightarrow \mathrm{He}^3 + \mathrm{n}$ (to measure fuel retention in the wall).

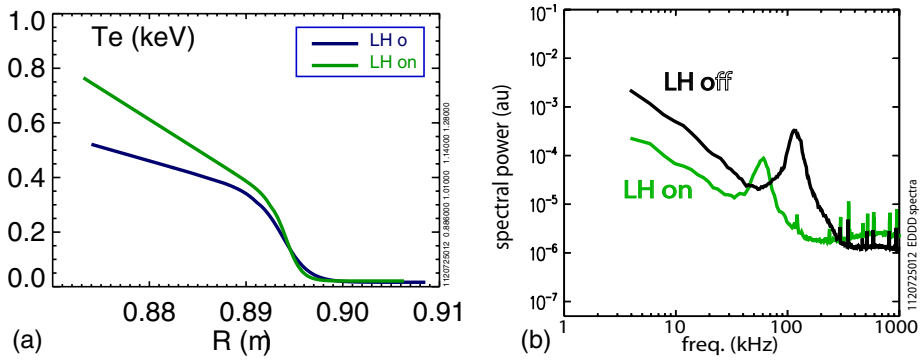

Figure 21. (*a*) The pedestal temperature profiles are modified and the total plasma energy content is increased with modest LH power (∼0.5 MW into a discharge with 3 MW of ICRH) under high-density conditions in which the plasma core is completely inaccessible to lower hybrid waves. (*b*) The increase in plasma temperature is accompanied by a sharp drop in edge fluctuations, suggesting a change in plasma transport. This may provide a novel mechanism for pedestal and confinement control.

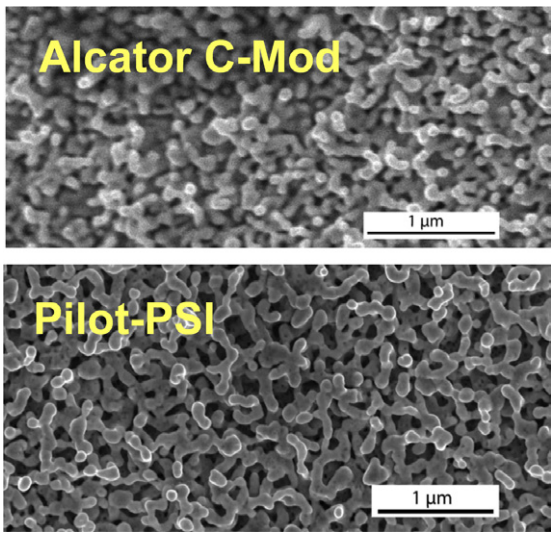

Figure 22. Tungsten nano-structures created in C-Mod and in the Pilot-PSI test stand are nearly identical in morphology and growth rate. Thus we conclude that the tokamak environment has little or no impact on tungsten fuzz growth when compared to linear plasma devices.

Early results are encouraging. For example, figure 23(*b*) shows the first γ-ray spectrum obtained with this new diagnostic. The boron peak can be used to calculate the thickness of the boron layer. Measurements currently take less than 5 min, allowing between-shot analysis. In a controlled experiment, the inner-wall coating was seen to be reduced by a factor of five over the course of a single run day. Modest upgrades to the beam and detector system will allow even shorter observation times and thus a wide range of wall positions to be measured between shots. Between runs, a significant fraction of the first wall could be interrogated.

7. Disruption mitigation

Disruptions are a critical issue for ITER. Disruption mitigation, using gas injection (MGI) [77], can limit some of the worst effects, but the ensuing radiation must be fairly uniform. A peaking factor greater than 2 could lead to local melting of beryllium on the ITER first wall. Experiments were carried out on C-Mod with a goal of characterizing and minimizing the asymmetry of energy deposition after MGI. Toroidal symmetry was studied with multiple gas injection ports and several arrays of XUV diodes [78]. With a single injection point, using an optimized mixture of argon and helium, the toroidal peaking factors, defined as the ratio of maximum to minimum radiation intensity was found to be in the range 1.2–2.3. The asymmetry depends sensitively on magnetic geometry, with higher asymmetry in low-elongation plasma and in higher q_{95} diverted plasmas. Using a second valve could dramatically reduce the asymmetry of radiation during the pre-thermal-quench phase, but only with carefully matched hardware and timing between the two valves (see figure 24). The effectiveness is less during the thermal quench itself—though this phase tends to show greater symmetry even with a single gas valve. The total energy loss during the pre-thermal quench on C-Mod is relatively small, but may be much more important on ITER. Asymmetry depends also, on the character of $n = 1$ MHD oscillations that associated with this phase of disruption evolution. Slower MHD growth rates in the pre-quench phase of the disruption are associated with greater asymmetry. Plasma shape and q affects the growth of $n = 1$ MHD modes and may provide an explanation of these dependences. The effects of MHD may dominate over the effects of symmetrizing the gas injection. These experiments are currently being modelled using the NIMROD extended MHD code [79].

8. Future plans

A number of significant upgrades have been planned for C-Mod. The most ambitious is a new high temperature tungsten divertor. The divertor is being designed for operation at 1000 K in order to provide data on hydrogen isotope retention under reactor relevant conditions. Tritium retention is an important issue for ITER and critical for future reactors. Measurements of retention in the relatively cold first wall structures of current machines are too high by orders of magnitude. The situation should improve markedly at higher temperature, but this has not been confirmed on an actual confinement experiment. In order to sustain the reactor level heat fluxes produced in C-Mod, the high heat-flux areas of this divertor will be continuous, that is without gaps or leading edges that can result in localized heating and melting. The mechanical design

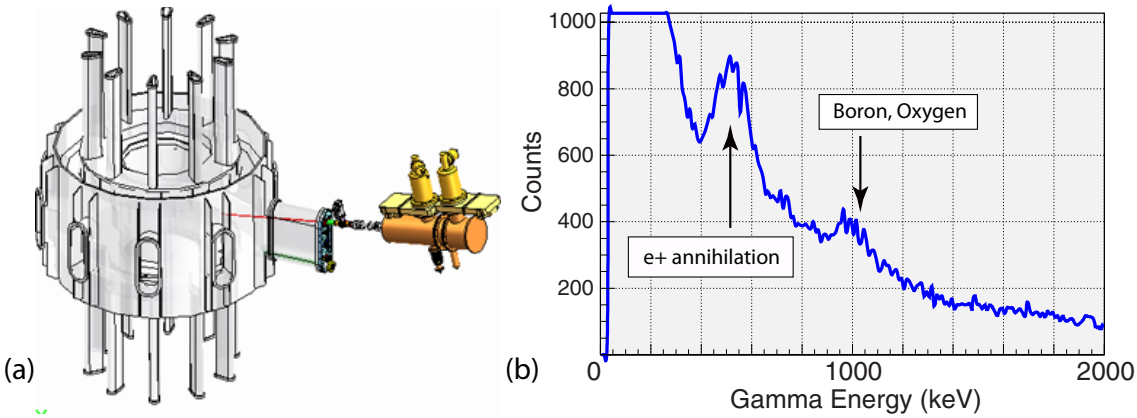

Figure 23. (*a*) A 1 MeV deuteron beam has been installed on C-Mod. With associated nuclear detectors, this has allowed the first ever, time-resolved, *in situ* measurements of plasma–wall processes. (*b*) This γ-ray spectra is the first obtained for this new diagnostic. It has allowed between-shot analysis of boron wall coating, showing the erosion of the coating during a single run day.

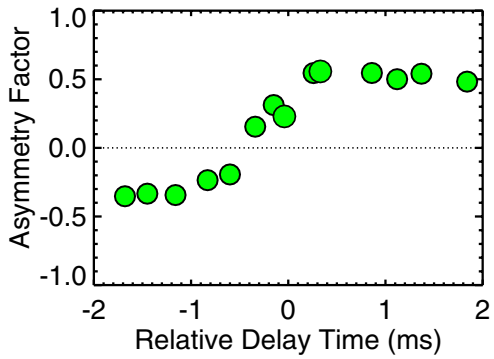

Figure 24. Radiation asymmetry during the pre-thermal quench (computed as the difference between two toroidal views divided by their sum) is plotted versus relative delay time between the firing of two gas valves used to mitigate disruptions.

is focused on maintaining a circular shape and alignment to a high degree of accuracy. Supplementing the divertor will be upgrades to the beam and detectors used for *in situ* measurement of plasma–wall processes, particularly hydrogen isotope retention—a major research thrust. A second field-aligned antenna will be installed, further reducing the radiated power and increasing the range of densities that can be heated at the highest powers. To improve current drive at high densities, a new LH launcher is under development. The RF waves will be launched above the outer midplane, following trajectories that bring them more directly to the core plasma and obviating edge parasitic losses. This second launcher will increase available LH power from 1 to 2 MW and by taking advantage of a velocity-space synergy, efficient current drive should be possible at densities above $10^{20}\,\mathrm{m}^{-3}$, enabling exploration of advanced non-inductive scenarios in ITER-relevant conditions. The launching structure combines the poloidal splitting concept of the current LH launcher [80] with a toroidal bi-junction [81].

Acknowledgments

The authors would like to thank the entire C-Mod team. This work is supported by the US Department of Energy.

References

[1] Ochoukov R., Whyte D., Faust I., LaBombard B., Meneghini O., Myra J., Wallace G. and Wukitch S. 2013 Investigation of RF-enhanced plasma potentials on Alcator C-Mod *J. Nucl. Mater.* at press doi:10.1016/j.jnucmat.2013.01.189
[2] Myra J.R. and D'Ippolito D.A. 2008 *Phys. Rev. Lett.* **101** 195004
[3] Cziegler I., Terry J., Wukitch S., Garrett M., Lau C. and Lin Y. 2012 *Plasma Phys. Control. Fusion* **54** 105019
[4] Garrett M. and Wukitch S. 2012 *Fusion Eng. Des.* **87** 1570
[5] Wukitch S. *et al* 2013 Evaluation of a field-aligned ICRF antenna in Alcator C-Mod *Phys. Plasmas* submitted
[6] Terry J., Cziegler I., Wukitch S., Garrett M., Lau C., Lin Y., Ochoukov R., Whyte D. and Zweben S. 2012 The fine-scale structure of the radial electric field in the SOL during ICRF heating on Alcator C-Mod *Proc. 24th Fusion Energy Conf. (San Diego, CA, 2012)* (Vienna: IAEA) and www-naweb.iaea.org/napc/physics/PS/conf.htm
[7] Brambilla M. 1999 *Plasma Phys. Control. Fusion* **41** 1
[8] Jaeger E.F., Berry L.A., D'Azevdo E., Batchelor D.B. and Carter M.D. 2001 *Phys. Plasmas* **8** 1573
[9] Harvey R.W. and McCoy M.G. 1992 CQL3D 1992 Fokker–Planck code *Proc. IAEA Technical Committee Meeting on Simulation and Modelling of Thermonuclear Plasmas (Montreal, Canada, 1992)* (USDOC NTIS Doc. No. D#93002962) p 40
[10] Tang V. *et al* 2007 *Plasma Phys. Control. Fusion* **49** 873
[11] Bader A., Bonoli P., Granetz R., Harvey R., Jaeger E., Parker R. and Wukitch S. 2011 Fast-ions on Alcator C-Mod: comparisons between simulation and experiment for equilibrium and evolving distributions *AIP Conf. Proc.* **1406** 357
[12] Porkolab M., Rost J., Basse N., Dorris J., Edlund E., Lin L., Lin Y. and Wukitch S. 2006 *IEEE Trans. Plasma Sci.* **34** 229
[13] Tsujii N., Prokolab M., Bonoli P., Lin Y., Wright J.C., Wukitch S., Jaeger E., Green D. and Harvey R. 2012 *Phys. Plasmas* **19** 082508
[14] Lin Y. *et al* 2009 *Phys. Plasmas* **16** 056102
[15] Lin Y., Granetz R., Reinke M., Rice J., Wolfe S. and Wukitch S. 2012 Characterization of NTMs in I-mode plasmas with ICRF mode conversion flow drive on Alcator C-Mod *Proc. 24th Fusion Energy Conf. (San Diego, CA, 2012)* (Vienna: IAEA) and www-naweb.iaea.org/napc/physics/PS/conf.htm
[16] LaHaye R.J., Buttery R., Guenter S., Huysmans G.T.A., Maraschek M. and Wilson H.R. 2000 *Phys. Plasmas* **7** 3349

[17] Meneghini O., Lau C., Shiraiwa S., Wallace G.M., Parker R.R., LaBombard B.L., Faust C., Wilson J.R. and Wukitch S. 2011 SOL effects on LH wave coupling and current drive performance on Alcator C-Mod *Proc. 19th Topical Conf. on Radio Frequency Power in Plasmas (Newport, RI, USA)*; *AIP Conf. Proc.* **1406** 411

[18] Lau C., Hanson G., Lin Y., Meneghini O., Wukitch S., Labombard B., Parker R., Shiraiwa S., Wallace G., Wilson J. and the Alcator C-Mod Team 2011 Effects of ICRF and LHCD on SOL density profiles on Alcator C-Mod *Proc. 19th Topical Conf. on Radio Frequency Power in Plasmas (Newport, RI, USA); AIP Conf. Proc.* **1406** 227

[19] Shiraiwa S. *et al* 2012 Progress toward steady-state regimes in Alcator C-Mod *Proc. 24th Fusion Energy Conf. (San Diego, CA, 2012)* (Vienna: IAEA) and www-naweb.iaea.org/napc/physics/PS/conf.htm

[20] Wallace G. *et al* 2012 *Phys. Plasmas* **19** 062505

[21] Smirnov A.P. and Harvey R. 1995 *Bull. Am. Phys. Soc.* **40** 1837

[22] Meneghini O., Shiraiwa S., Faus I., Parker R., Schmidt A. and Wallace G. 2011 *Fusion Sci. Technol.* **60** 40

[23] Wallace G. *et al* 2010 *Phys. Plasmas* **17** 082508

[24] James A., Soukhanovskii V., Churchill M., Lipschultz B., Miller D., Reinke M., Terry J. and Theiler C. 2012 *Bull. Am. Phys. Soc.* **57** 140

[25] Bertelli N *et al* 2012 The effects of the scattering by edge plasma density fluctuations on LH wave propagation, PPPL-4801

[26] Takase Y., Porkolab M., Schuss J., Watterson R., Firoe C., Slusher R. and Surko C. 1985 *Phys. Fluids* **28** 983

[27] Wallace G. *et al* 2012 Advance in LHCD technology on Alcator C-Mod *Proc. 24th Fusion Energy Conf. (San Diego, CA, 2012)* (Vienna: IAEA) and www-naweb.iaea.org/napc/physics/PS/conf.htm

[28] White A.E. *et al* 2008 *Phys. Plasmas* **15** 056116

[29] Holland C., White A., McKee G., Shafer M., Candy J., Waltz R., Schmitz L. and Tynan G. 2009 *Phys. Plasmas* **16** 052301

[30] Rhodes T.L. *et al* 2011 *Nucl. Fusion* **51** 063022

[31] Candy J. and Waltz R. 2003 *J. Comput. Phys.* **186** 545

[32] White A.E. *et al* 2012 Multi-channel transport experiments at Alcator C-Mod and comparison with gyrokinetic simulations *Phys. Plasmas* submitted

[33] Waltz R. *et al* 2012 Search for the missing L-mode edge transport and possible breakdown of gyrokinetics *Phys. Plasmas* submitted

[34] Howard N.T., Greenwald M. and Rice J. 2011 *J. Rev. Sci. Instrum.* **82** 033512

[35] Howard N.T., Greenwald M., Mikkelsen D., Reinke M., White A., Ernst D., Podpaly Yu. and Candy J. 2012 *Nucl. Fusion* **52** 063002

[36] Howard N.T., Greenwald M., Mikkelsen D., White A., Reinke M., Ernst D., Podpaly Yu. and Candy J. 2012 *Phys. Plasmas* **19** 056110

[37] Reinke M., Hutchinson I., Rice J., Howard N., Bader A., Wukitch S., Lin Y., Pace D., Hubbard A., Hughes J. and Podpaly Yu. 2012 *Plasma Phys. Control. Fusion* **54** 045004

[38] Rice J. *et al* 2011 *Nucl. Fusion* **51** 083005

[39] Rice J. *et al* 2011 *Phys. Rev. Lett.* **107** 265001

[40] Rice J.E. *et al* 2013 *Nucl. Fusion* **53** 033004

[41] Gentle K.W. *et al* 1995 *Phys. Plasmas* **2** 2292

[42] Fiore C. *et al* 2012 *Phys. Plasmas* **19** 056113

[43] Kotschenreuther M., Rewoldt G. and Tang W.M. 1995 *Comput. Phys. Commun.* **88** 128

[44] Ernst D.R., Basse N., Dorland W., Fiore C., Lin L., Long A., Porkolab M., Zeller K. and Zhurovich K. 2006 *Proc. 21st Fusion Energy Conf. (Chengdu, China)* (Vienna: IAEA) CD-ROM file TH/1-3 and http://www-naweb.iaea.org/napc/physics/fec/fec2006/html/index.html

[45] Ernst D.R. *et al* 2004 *Phys. Plasmas* **11** 2637

[46] Ernst D. *et al* 2012 Nonlinear upshift of trapped electron mode critical density gradient: simulation and experiment *Phys. Plasmas* submitted

[47] Whyte D. *et al* 2010 *Nucl. Fusion* **50** 105005

[48] Hubbard A. *et al* 2011 *Phys. Plasmas* **18** 056115

[49] Walk J.R., Snyder P., Hughes J., Terry J., Hubbard A. and Phillips P. 2012 *Nucl. Fusion* **52** 063011

[50] Hughes J.W. *et al* 2012 Pedestal stability and transport on the Alcator C-Mod tokamak: experiments in support of developing predictive capability *Proc. 24th Fusion Energy Conf. (San Diego, CA)* (Vienna: IAEA) and www-naweb.iaea.org/napc/physics/PS/conf.htm

[51] Snyder P.B., Groebner R.J., Hughes J.W., Osborne T.H., Beurskens M., Leonard A.W., Wilson H.R. and Xu X.Q. 2011 *Nucl. Fusion* **51** 103016

[52] Martin Y., Takizuka T. and the ITPA CDBM Threshold Database Working Group 2008 *Proc. 11th IAEA Technical Meeting on H-mode Physics; J. Phys.: Conf. Ser.* **123** 012033

[53] Ma Y., Hughes J.W., Hubbard A., LaBombard B., Churchill R., Golfinopolous T., Tsujii N. and Marmar E. 2012 *Nucl. Fusion* **52** 023010

[54] Greenwald M., Terry J.L., Wolfe S.M., Ejima S., Bell M.G., Kaye S.M. and Neilson G.H. 1988 *Nucl. Fusion* **28** 2199

[55] Fundamenski W., Militello F., Moulton D. and McDonald D.C. 2012 *Nucl. Fusion* **52** 062003

[56] Rogers B., Drake J. and Zeiler A. 1998 *Phys. Rev. Lett.* **81** 4396

[57] Wilson H.R., Snyder P.B., Huysmans G.T.A. and Miller R.L. 2002 *Phys. Plasmas* **9** 1277

[58] Greenwald M. *et al* 1999 *Phys. Plasmas* **6** 1943

[59] Dominguez A., Terry J., LaBombard B., Marmar E., Greenwald M., Hubbard A., Hughes J., Kramer G., White A. and Whyte D. 2012 Particle transport and the weakly coherent mode in I-mode plasmas *Nucl. Fusion* submitted

[60] Cziegler I. *et al* 2012 Fluctuating zonal flows in I-mode in Alcator *Phys. Plasmas* submitted

[61] LaBombard B. *et al* 2011 *Phys. Plasmas* **18** 056104

[62] Brunner D. and LaBombard B. 2012 *Rev. Sci. Instrum.* **83** 033501

[63] Brunner D. *et al* 2013 Divertor 'death-ray' explained *J. Nucl. Mater.* at press doi:10.1016/j.jnucmat.2013.01.264

[64] Whyte D. *et al* 2013 Constraining divertor heat-width in ITER *J. Nucl. Mater.* at press doi:10.1016/j.jnucmat.2013.01.088

[65] Eich T. *et al* 2012 Scaling of the SOL H-mode power width *Proc. 24th Fusion Energy Conf. (San Diego, CA)* (Vienna: IAEA) and www-naweb.iaea.org/napc/physics/PS/conf.htm

[66] Terry J., LaBombard B., Brunner D., Hughes J., Reinke M. and Whyte D. 2012 Heat-flux widths and power flows during H-mode and I-mode operation in Alcator C-Mod *J. Nucl. Mater.* at press doi:10.1016/j.jnucmat.2013.01.029

[67] Loarte A. *et al* 2011 *Phys. Plasmas* **18** 056105

[68] Maqueda R. *et al* 2003 *Rev. Sci. Instrum.* **74** 2020

[69] Garcia O.E., Cziegler I., Kube R., LaBombard B. and Terry J. 2013 Burst statistics in Alcator C-Mod SOL turbulence *J. Nucl. Mater.* at press doi:10.1016/j.jnucmat.2013.01.054

[70] Garcia O.E. 2012 *Phys. Rev. Lett.* **108** 265001

[71] Garcia O.E. *et al* 2012 Intermittent fluctuations in the Alcator C-Mod scrape-off layer *Phys. Plasmas* submitted

[72] Hughes J.W. *et al* 2010 *Nucl. Fusion* **50** 064001

[73] Woller K.B., Whyte D., Wright G., Doerner R. and de Temmerman G. 2012 Depth profiles of helium and hydrogen in tungsten nano-tendril surface morphology *J. Nucl. Mater.* at press doi:10.1016/j.jnucmat.2013.01.198

[74] Wright G.M., Brunner D., Baldwin M., Doerner R., LaBombard B., Lipschultz B., Terry J. and Whyte D. 2012 *Nucl. Fusion* **52** 042003

[75] Wright G.M. *et al* 2013 Comparison of tungsten nano-tendrils grown in Alcator C-Mod and linear plasma devices *J. Nucl. Mater.* at press doi:10.1016/j.jnucmat.2013.01.013

[76] Hartwig Z.S. and Whyte D.G. 2010 *Rev. Sci. Instrum.* **81** 10E106
[77] Granetz R.S. *et al* 2007 *Nucl. Fusion* **47** 1086
[78] Olynyk G.M. *et al* 2013 Disruption mitigation experiments with multiple gas jets on Alcator C-Mod *Nucl. Fusion* at press
[79] Izzo V.A., Whyte D.G., Granetz R.S., Parks P.B., Hollmann E.M., Lao L.L. and Wesley J.C. 2008 *Phys. Plasmas* **15** 056109
[80] Shiraiwa S. *et al* 2011 *Nucl. Fusion* **51** 103024
[81] Moreau D. and Nguyen T.K. 1984 *Proc. 6th Joint Kiev Conf. (Lausanne, Switzerland, 1984)*; *Plasma Phys.* **1** 216